

# UC Berkeley

## UC Berkeley Previously Published Works

### Title

Anomalously Suppressed Thermal Conduction by Electron-Phonon Coupling in Charge-Density-Wave Tantalum Disulfide

### Permalink

<https://escholarship.org/uc/item/2hx2h80r>

### Journal

Advanced Science, 7(11)

### ISSN

2198-3844

### Authors

Liu, Huili  
Yang, Chao  
Wei, Bin  
et al.

### Publication Date

2020-06-01

### DOI

10.1002/advs.201902071

Peer reviewed

# Anomalously Suppressed Thermal Conduction by Electron-Phonon Coupling in Charge-Density-Wave Tantalum Disulfide

Huili Liu, Chao Yang, Bin Wei, Lei Jin, Ahmet Alatas, Ayman Said, Sefaattin Tongay, Fan Yang, Ali Javey, Jiawang Hong,\* and Junqiao Wu\*

Charge and thermal transport in a crystal is carried by free electrons and phonons (quantized lattice vibration), the two most fundamental quasiparticles. Above the Debye temperature of the crystal, phonon-mediated thermal conductivity ( $\kappa_L$ ) is typically limited by mutual scattering of phonons, which results in  $\kappa_L$  decreasing with inverse temperature, whereas free electrons play a negligible role in  $\kappa_L$ . Here, an unusual case in charge-density-wave tantalum disulfide (1T-TaS<sub>2</sub>) is reported, in which  $\kappa_L$  is limited instead by phonon scattering with free electrons, resulting in a temperature-independent  $\kappa_L$ . In this system, the conventional phonon–phonon scattering is alleviated by its uniquely structured phonon dispersions, while unusually strong electron-phonon (e-ph) coupling arises from its Fermi surface strongly nested at wavevectors in which phonons exhibit Kohn anomalies. The unusual temperature dependence of thermal conduction is found as a consequence of these effects. The finding reveals new physics of thermal conduction, offers a unique platform to probe e-ph interactions, and provides potential ways to control heat flow in materials with free charge carriers. The temperature-independent thermal conductivity may also find thermal management application as a special thermal interface material between two systems when the heat conduction between them needs to be maintained at a constant level.

Interactions between free electrons and lattice vibration (phonons) in metallic conductors lead to their electrical conductivity decreasing with temperature, an effect that is widely observed and well understood.<sup>[1,2]</sup> However, effects of electron-phonon (e-ph) interaction on materials' thermal conductivity are not understood as well, and have been experimentally elusive.<sup>[3,4]</sup> In electrical conductors, in addition to directly conducting heat themselves (contributing to thermal conductivity with the electronic part,  $\kappa_e$ ), free charge carriers also couple with and scatter phonons, hence reducing  $\kappa_L$ . The reduction in  $\kappa_L$  arising from e-ph coupling is typically weak as a very high density ( $>\approx 10^{20}$  cm<sup>-3</sup>) of electrons is needed,<sup>[4]</sup> hence in nonmetallic systems where carrier density is lower, it is hard to be experimentally detected. In metallic systems with very high charge carrier densities, the e-ph scattering could rise to levels that considerably reduce  $\kappa_L$ , but the measured total thermal conductivity  $\kappa = \kappa_e + \kappa_L$  would then be dominated by the contribution of  $\kappa_e$  instead. Experimental exploration of the effects of e-ph scattering on thermal

Dr. H. Liu, L. Jin, Prof. A. Javey, Prof. J. Wu  
Materials Sciences Division  
Lawrence Berkeley National Laboratory  
Berkeley, CA 94720, USA  
E-mail: wuj@berkeley.edu

Dr. H. Liu, L. Jin, Prof. J. Wu  
Department of Materials Science and Engineering  
University of California  
Berkeley, CA 94720, USA


Dr. C. Yang, B. Wei, Prof. J. Hong  
School of Aerospace Engineering  
Beijing Institute of Technology  
Beijing 100081, China  
E-mail: hongjw@bit.edu.cn

Dr. A. Alatas, Dr. A. Said  
Advanced Photon Source  
Argonne National Laboratory  
Lemont, IL 60439, USA

Prof. S. Tongay  
School for Engineering of Matter, Transport, and Energy  
Arizona State University  
Tempe, AZ 85287, USA

Prof. F. Yang  
Department of Mechanical Engineering  
Stevens Institute of Technology  
Hoboken, NJ 07030, USA

Prof. A. Javey  
Department of Electrical Engineering and Computer Science  
University of California  
Berkeley, CA 94720, USA

 The ORCID identification number(s) for the author(s) of this article can be found under <https://doi.org/10.1002/advs.201902071>

© 2020 The Authors. Published by WILEY-VCH Verlag GmbH & Co. KGaA, Weinheim. This is an open access article under the terms of the Creative Commons Attribution License, which permits use, distribution and reproduction in any medium, provided the original work is properly cited.

DOI: 10.1002/advs.201902071

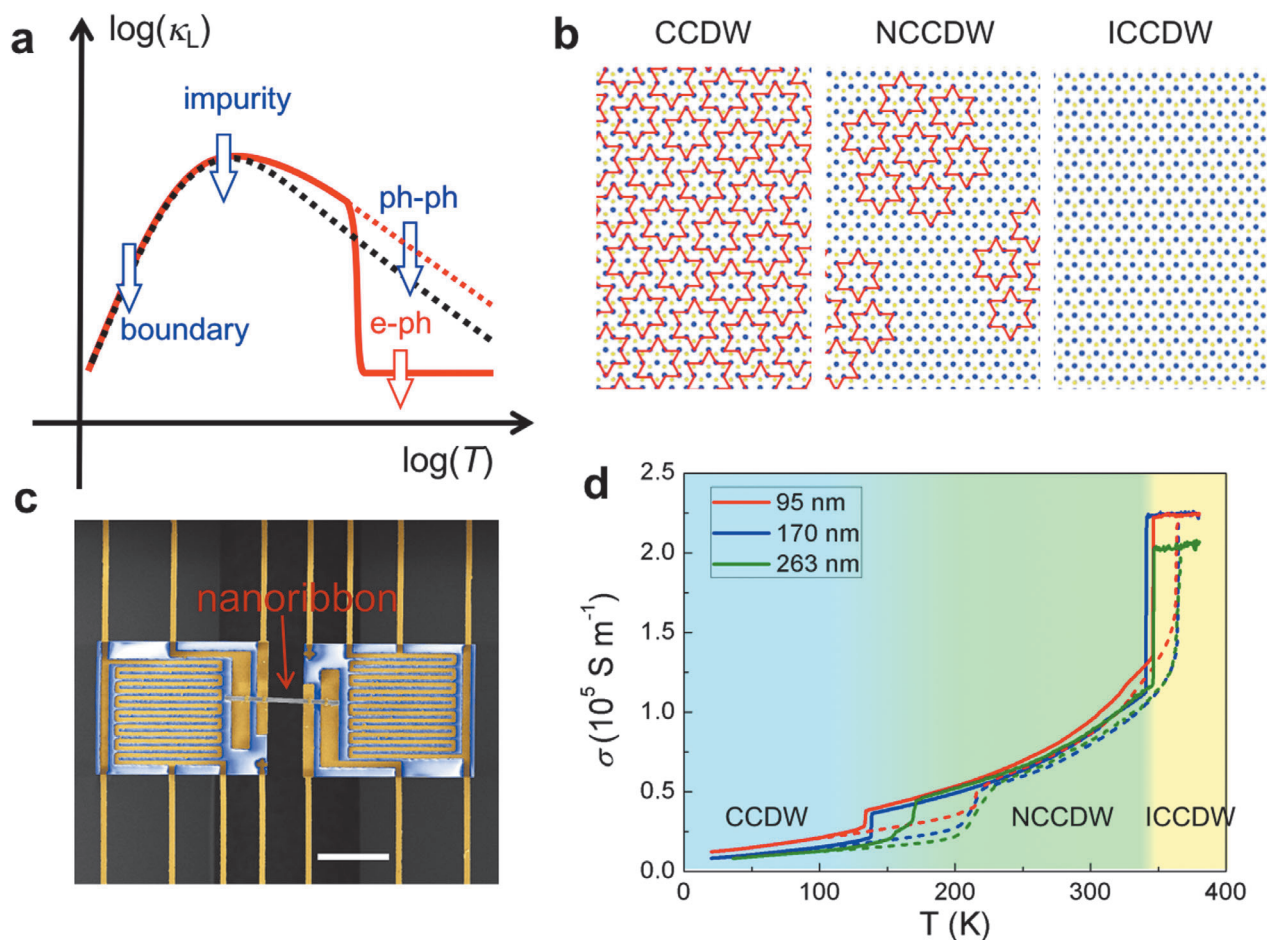


**Figure 1.** CDW in 1T-TaS<sub>2</sub> and nanoribbon devices for electrical and thermal measurements. a) The effect compared to conventional cases: in conventional materials (black dashed line) at high temperatures, lattice thermal conductivity ( $\kappa_L$ ) is limited by ph-ph scattering resulting in an  $1/T$  dependence, while the effect of e-ph scattering is negligible; the opposite is observed in this work, where ph-ph scattering is intrinsically weak (red dashed line) while e-ph scattering dominantly limits the thermal conductivity, leading to  $T$ -independent  $\kappa_L$  (solid red line). Major phonon scattering mechanisms at low (boundary) and intermediate (impurity) temperatures are also indicated. b) Schematic charge-density-wave structures with different levels of commensuration (commensurate as CCDW, nearly commensurate as NCCDW, incommensurate as ICCDW). Red “David stars” represent displacement patterns of Ta atoms. c) False-color SEM image of two suspended pads bridged with a TaS<sub>2</sub> nanoribbon that is FIB-bonded onto the underlying Pt electrodes. Scale bar: 20  $\mu\text{m}$ . d) Temperature dependence of electrical conductivity of TaS<sub>2</sub> nanoribbons with different thicknesses measured with a four-probe geometry. Solid lines are for cooling and dashed lines are for warming.

transport has been limited to metallic systems at very low temperatures<sup>[5]</sup> because of the difficulty in separating  $\kappa_L$  from  $\kappa_e$ .

Indeed, recently Liao et al.<sup>[4]</sup> calculated that  $\kappa_L$  of silicon can be reduced by up to  $\approx 45\%$  in the presence of a high density ( $\approx 10^{21} \text{ cm}^{-3}$ ) of free charge carriers. It has also been proposed that e-ph coupling may be responsible for unusually low values of  $\kappa$  observed in VN<sub>x</sub>.<sup>[6]</sup> Yang et al. reported  $\kappa_L$  reduced in NbSe<sub>3</sub> nanowires beyond conventional phonon scattering mechanisms that is attributed to e-ph coupling.<sup>[7]</sup> Theoretical calculations done by Li et al. show that group-V transition metal carbides (VC, NbC, and TaC) host intrinsically strong e-ph coupling and weak ph-ph scattering, leading to  $\kappa_L$  theoretically much lower than the case when the e-ph coupling is absent.<sup>[8]</sup> As schematically shown in **Figure 1a**, we discover direct experimental evidence of  $\kappa_L$  dominated by e-ph scattering rather than the conven-

tional ph-ph scattering, in a charge-density-wave material, tantalum disulfide (TaS<sub>2</sub>).

As a layered material, the octahedral (1T) polytype of TaS<sub>2</sub> features a well-known series of charge density wave (CDW) phase transitions.<sup>[9–11]</sup> Above  $\approx 550 \text{ K}$ , it takes the normal, metallic phase with the space group of  $P\bar{3}m1$ . At lower temperatures, CDW phases show up with distinct commensurations with the underlying lattice: an incommensurate (ICCDW) phase above  $\approx 350 \text{ K}$ , a nearly commensurate (NCCDW) phase between  $\approx 150$  and  $\approx 350 \text{ K}$ , and a commensurate (CCDW) phase below  $\approx 150 \text{ K}$ . As schematically shown in **Figure 1b**, in the CCDW phase, the CDW distortion of atoms forms “David-stars” resulting in an ordered  $\sqrt{13} \times \sqrt{13}$  superlattice structure. The CDW deformation induces a sizeable energy gap in the electronic band structure.<sup>[12]</sup> In the NCCDW phase, domains of David-star clusters are isolated from each other by a metallic network, where

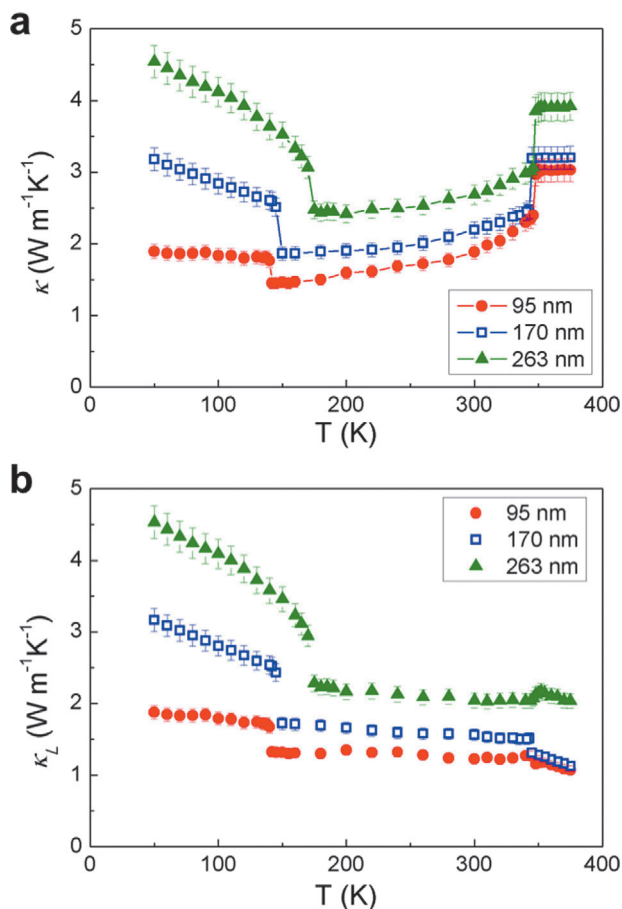


**Figure 2.** Measured thermal conductivity of TaS<sub>2</sub> nanoribbons. a)  $T$  dependence of total thermal conductivity ( $\kappa$ ) of nanoribbons with different thicknesses. b) Lattice thermal conductivity ( $\kappa_L$ ) calculated by subtracting the electron contribution ( $\kappa_e$ ) from  $\kappa$  assuming the Wiedemann–Franz law.

electrons behave itinerant. The CDW phases in 1T-TaS<sub>2</sub> are correlated with the lattice deformation and simultaneously a Fermi surface instability,<sup>[13]</sup> where electrons and phonons are strongly coupled to shape its physical properties.

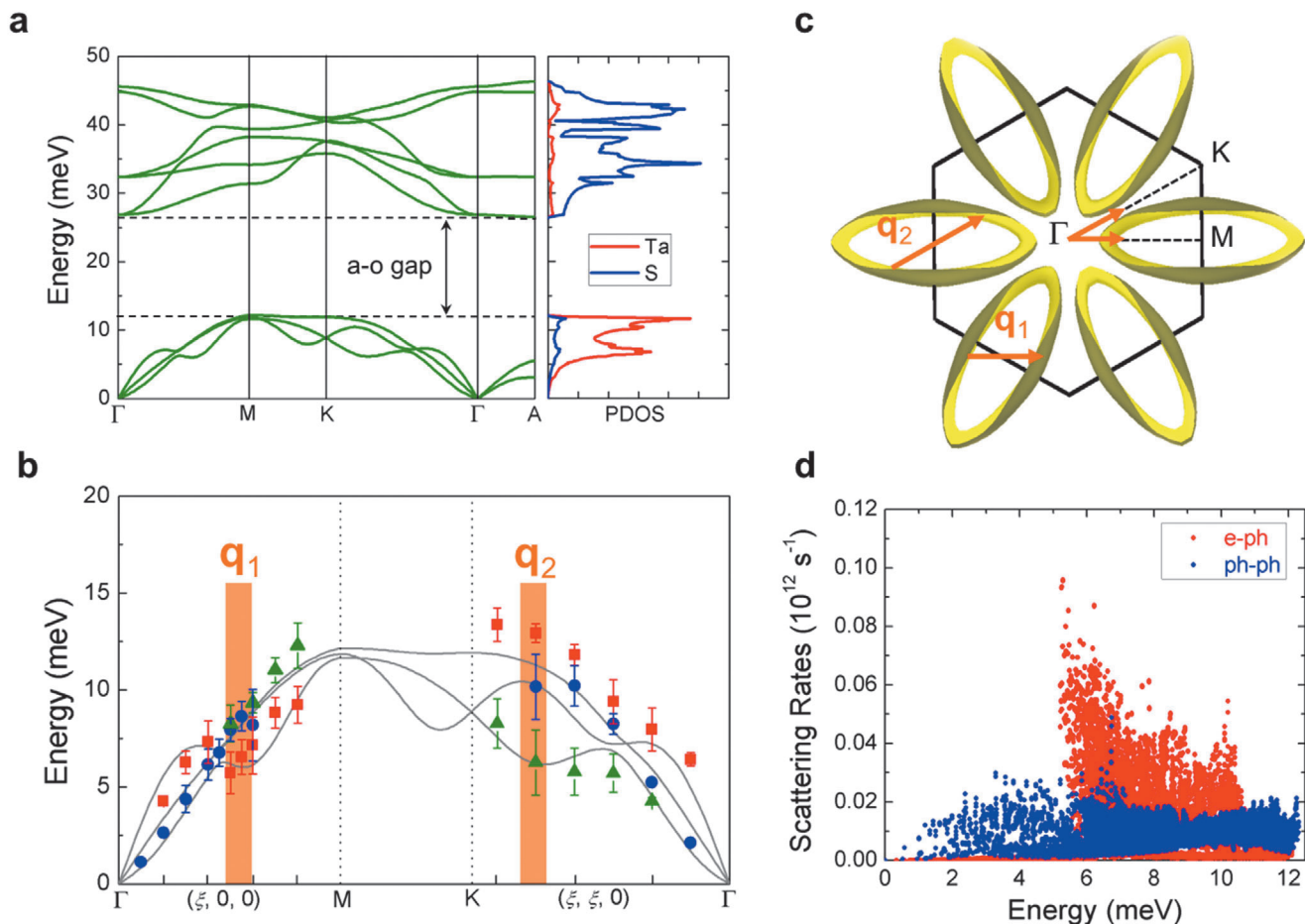
Figure 1c shows the image of a device for electrical and thermal measurements. 1T-TaS<sub>2</sub> nanoribbons were fabricated from microflakes mechanically exfoliated out of bulk crystals and measured following the method published previously<sup>[14,15]</sup> (see details in Experimental Section). Electrical conductivity ( $\sigma$ ) of nanoribbons with different thicknesses is shown in Figure 1d. The three phases (CCDW, NCCDW, and ICCDW) are clearly separated in conductivity at the transition temperature of  $\approx 150$  and  $\approx 350$  K, respectively, with a hysteresis at each transition. Experimentally, it has been reported in bulk 1T-TaS<sub>2</sub> samples that the CCDW phase is a semiconductor and the NCCDW phase is effectively a semimetal,<sup>[16]</sup> and their carrier density is on the order of  $\approx 1 \times 10^{19}$  and  $\approx 1 \times 10^{22} \text{ cm}^{-3}$ , respectively.<sup>[17]</sup>

Figure 2a shows measured  $\kappa$  over all three phases, qualitatively consistent with that of bulk samples.<sup>[18,19]</sup> In addition to a clear overall reduction of  $\kappa$  with nanoribbon thickness, abrupt jumps at each of the phase transition temperature are evident.

To extract  $\kappa_L$ , we calculate  $\kappa_e$  using Wiedemann–Franz law ( $\kappa_e = L\sigma T$ ), where the Lorenz ratio  $L$  takes the Sommerfeld value of  $L_0 \equiv 2.44 \times 10^{-8} \text{ W } \Omega \text{ K}^{-2}$ , and subtract  $\kappa_e$  out of the measured  $\kappa$ . The obtained  $\kappa_L$  is shown in Figure 2b. A significant reduction in  $\kappa_L$  between the CCDW and NCCDW phases is observed at the phase transition temperature around 150 K. More interestingly, in the entire NCCDW phase between  $\approx 150$  and  $\approx 350$  K,  $\kappa_L$  becomes nearly  $T$ -independent. Since the Debye temperature of 1T-TaS<sub>2</sub> is about 172 K,<sup>[20]</sup> in the NCCDW temperature range,  $\kappa_L$  is expected to be limited by momentum-nonconserving ph-ph scattering (the Umklapp process), which would result in an  $1/T$  dependence as depicted in Figure 1a (black dashed line). The  $T$  independence of  $\kappa_L$ , therefore, suggests unconventional phonon scattering mechanisms dominating the Umklapp process in this material.

To suppress the ph-ph scattering, specific phonon dispersions are required to limit the scattering phase space.<sup>[8]</sup> Due to the lack of long-range order of the lattice structure in the NCCDW and ICCDW phases, we examine phonon dispersions of the normal phase from the first-principles calculation (see details in Experimental Section), to provide insights to the NCCDW phase under investigation. Indeed, recent results from angular-resolved photoelectron spectroscopy shows electronic band structure of NCCDW phase largely in agreement with first-principles calculations based on the normal phase.<sup>[16]</sup> As shown later, the phonon dispersions we calculated for the normal phase (Figure 3a) are also in good agreement with inelastic X-ray scattering (IXS) measurements of the NCCDW phase. Two general features are clearly seen in Figure 3a: (1) the acoustic-optical (a-o) phonon gap is unusually wide, nearly equal to the bandwidth of the acoustic phonons, similar to the case of BaS<sup>[21–24]</sup> and NbC,<sup>[8]</sup> and (2) the acoustic phonon dispersions are tightly bunched together. The effect (1) of wide phonon gap is attributed to the large mass ratio in TaS<sub>2</sub> ( $m_{\text{Ta}}/m_{\text{S}} \approx 5.7$ ),<sup>[25]</sup> as Ta and S are responsible mostly for the acoustic and optical modes, respectively (Figure 3a). Such an a-o bandgap wider than the maximal acoustic phonon energy prohibits the phonon scattering process that involves two acoustic and one optical phonons (the so-called *aa*o process).<sup>[21]</sup> The effect (2) of acoustic phonon bunching significantly limits the phonon scattering process involving three acoustic phonons (the *aaa* process) by reducing the scattering phase space.<sup>[21]</sup> As a result, the Umklapp process of ph-ph scattering is greatly suppressed, making room for thermal phonons to be dominantly scattered by other  $T$ -independent mechanisms.

To understand phonon properties in the NCCDW phase, we measured the acoustic phonon dispersions using IXS (see details in Experimental Section). The phonon dispersions measured at 300 K along  $\Gamma$ -M and  $\Gamma$ -K directions are shown in Figure 3b with the underlying calculated dispersions (solid line). It can be seen that these transverse acoustic (TA) and longitudinal acoustic (LA) phonon dispersions are indeed bunched together as shown from density functional theory (DFT) calculation. Secondly, Kohn anomalies<sup>[26]</sup> are observed in the dispersions. For example, along the  $\Gamma$ -M direction, the LA phonon shows phonon softening at wavevector  $q_1 \approx 0.6 q_{\Gamma\text{-M}}$ , consistent with neutron scattering measurements.<sup>[27]</sup> Along the  $\Gamma$ -K direction, the TA phonon modes also show broad, flat regions at certain range of wavevectors denoted as  $q_2$ . Interestingly, these less-dispersive modes generally show larger linewidths ( $\Gamma$ ) than



**Figure 3.** Phonon dispersion and Fermi surface featuring weak ph-ph scattering and strong e-ph coupling. a) Phonon dispersion of the normal phase from DFT calculations, and partial PDOS of 1T-TaS<sub>2</sub> involving vibration of Ta and S atoms, respectively. The large a-o phonon gap and bunched acoustic phonons suppress ph-ph scattering. A high PDOS peak is seen between 6 and 8 meV, corresponding to the less-dispersive phonon modes. b) Acoustic phonon dispersion (points) of the NCCDW phase measured at 300 K by IXS, overlaid onto the calculated dispersion (solid lines) in (a). The measured phonon linewidth is represented by the error bars. The phonon anomalies along the  $\Gamma$ -M and  $\Gamma$ -K directions are clearly seen, where the linewidth is unusually broadened. c) Calculated electron Fermi surface of 1T-TaS<sub>2</sub> in the normal phase, which is nested with the two wavevectors  $q_1$  and  $q_2$  along the  $\Gamma$ -M and  $\Gamma$ -K directions, respectively. These two wavevectors are correlated to the phonon anomalies shown in (b), enabling strong e-ph coupling. d) Calculated e-ph (red points) and ph-ph (blue points) scattering rates as a function of phonon energy, showing e-ph scattering rates higher than ph-ph rates for phonon modes between  $\approx 6$  and 8 meV.

dispersive modes at comparable energies, as shown in Figure S5, Supporting Information. Since the phonon linewidth is related to phonon scattering rate ( $1/\tau$ ) via the uncertainty principle,  $\Gamma \propto 1/\tau$ , the experimental data in Figure 3b indicate that the acoustic phonons are unusually strongly scattered near those wavevectors.

To elucidate the mechanism of the momentum-selective phonon scattering, we calculated the Fermi surface of electrons in TaS<sub>2</sub>, which is shown in Figure 3c and Figure S6, Supporting Information. On the Fermi surface, there exist regions with large areas that are parallel to each other; hence, it is strongly nested with certain fixed wavevectors  $q$ . The nesting allows free electrons to be strongly scattered on the Fermi surface if a momentum  $\hbar q$  is externally provided by phonons. Interestingly, the shape of the Fermi surface in Figure 3c features two nesting wavevectors along the  $\Gamma$ -M and  $\Gamma$ -K directions, respectively, quantitatively consistent with the anomaly wavevectors ( $q_1$  and  $q_2$ ) observed in the phonon dispersions in Figure 3b. This agreement is a proof of

strong coupling between free electrons and acoustic phonons. The e-ph scattering rate for the phonon mode  $j$  with wavevector  $q$  is given by<sup>[1,8]</sup>

$$\frac{1}{\tau_{e-ph}} \propto \sum_{mn} \int d\mathbf{k} |g_{nmj}^{e-ph}(\mathbf{k}, \mathbf{q})|^2 [f_0(\epsilon_{nk}) - f_0(\epsilon_{mk+q})] \times \delta(\epsilon_{mk+q} - \epsilon_{nk} - \hbar\omega_{jq}) \quad (1)$$

where  $\epsilon_{nk}$  and  $\epsilon_{mk+q}$  are electron energies in the initial ( $n, \mathbf{k}$ ) and the final ( $m, \mathbf{k}+\mathbf{q}$ ) states,  $\hbar\omega_{jq}$  is energy of the phonon in the state ( $j, \mathbf{q}$ ),  $f_0$  is Fermi distribution,  $g_{nmj}^{e-ph}(\mathbf{k}, \mathbf{q})$  is e-ph scattering matrix element, and the sums are over the electron bands  $n$  and  $m$ . When the Fermi surface is nested with a wavevector  $q$ , phonon modes with momentum  $\hbar q$  and energy  $\hbar\omega_{jq}$  will be strongly scattered due to the large phase space available in the integration. This is the case for phonon modes near the Kohn anomaly wavevectors



$q_1$  and  $q_2$ , which are relatively less dispersive and contribute a high phonon density of states (PDOS) between  $\approx 6$  and 8 meV (Figure 3a). Acoustic phonon modes at other wavevectors, especially those with smaller wavevectors, experience much weaker scattering rates. This is experimentally evidenced from the very narrow linewidths for phonon modes near the  $\Gamma$  point observed in IXS experiments (Figure 3b). Indeed, as shown in Figure 3d, first-principles calculations confirm that the e-ph scattering rates are considerably stronger than ph-ph scattering rates for acoustic phonon modes of energy higher than 5 meV, especially those between 6 and 8 meV, corresponding to the less dispersive modes near  $q_1$  and  $q_2$ .

The unusual temperature-independent thermal conductivity results fundamentally from a nested Fermi surface interplaying with uniquely structured phonon dispersions. These conditions could be met in metallic compounds with large cation/anion mass ratios and signatures of strong e-ph coupling such as superconductivity and CDWs. As high density of charge carriers can be introduced by a gate field via either electrostatics or field-induced insulator to metal transition,<sup>[11,28]</sup> the effect also reveals a potential way to electrically and locally tune thermal conduction of solids for nonlinear thermal devices.<sup>[29,30]</sup> New exotic physics of 1T-TaS<sub>2</sub>, such as quantum spin liquid state,<sup>[31]</sup> may also need to be invoked as possible additional heat carriers. We also note the complication that in the case of very strong e-ph coupling, a complete separation between lattice and electronic thermal conductivity may not always be possible.<sup>[32]</sup> We further state that the honeycomb domain walls network of topological excitations in NCCDW phase identified recently<sup>[33]</sup> may provide new phonon modes for heat conduction in 1T-TaS<sub>2</sub>.

## Experimental Section

**1T-TaS<sub>2</sub> Nanoribbons Device Fabrication:** 1T-TaS<sub>2</sub> flakes were mechanically exfoliated onto a SiO<sub>2</sub>/Si substrate using polydimethylsiloxane, and then nanoribbons (1–2  $\mu\text{m}$  in width and 25–40  $\mu\text{m}$  in length) were produced using electron-beam lithography (EBL) followed by reactive ion etching.<sup>[15,34]</sup> The flakes were spin coated by poly(methyl methacrylate) (PMMA, C4-950, 4000 rpm) and baked at 180 °C for 5 min. The PMMA was patterned with EBL, followed by a developing process using methyl isobutyl ketone/isopropyl alcohol (IPA) = 1:3 for 1 min. The exposed TaS<sub>2</sub> was etched via reactive ion etching using a mixed gas (90% SF<sub>6</sub> and 10% O<sub>2</sub>, 60 sccm) for several seconds. After the PMMA removal with acetone and rinsing by isopropyl alcohol, TaS<sub>2</sub> nanoribbons were obtained. Four Ti/Au electrodes were then deposited onto the nanoribbons. To achieve that, a second EBL process was used to expose the electrode areas on the nanoribbons. The exposed areas were Ar<sup>+</sup> milled (30–60 s) to remove any oxidized or contaminated layer on the surface, and then coated with Ti (10 nm, deposition rate  $\approx 0.5 \text{ \AA s}^{-1}$ ) and Au (70 nm, deposition rate  $\approx 1 \text{ \AA s}^{-1}$ ) metals using electron beam evaporation (CHA Solution E-beam evaporator). A lift-off process was performed in acetone for  $\approx 5$  min with gentle shaking, followed by thorough rinsing with IPA. After that, the selected individual TaS<sub>2</sub> nanoribbon was manually picked up using a sharp tungsten needle (600 nm tip diameter, Cascade Microtech) in a micromanipulator probe station, and transferred onto an empty, suspended-pad microdevice, aligning the four Ti/Au metal electrodes of the nanoribbon onto the four Pt electrodes on the suspended pads. A small amount of Pt was then deposited along the edge of the predeposited Ti/Au electrodes, to bond them onto the underlying Pt electrodes using a focused ion beam (FIB) (dual-beam FEI Quanta). Such two-step contact formation ensures both good ohmic electrical conduction and negligible thermal resistance of the contacts, while minimizing exposure time to the FIB and the resul-

tant sample damage. Figure S1, Supporting Information, shows schematically the fabrication process and images of a nanoribbon device. The thickness of the nanoribbon was confirmed by atomic force microscopy (AFM) as shown in Figure S1b, Supporting Information. A scanning electron microscopy (SEM) image of the device is shown in Figure 1c. After Pt deposition, electrical quality of the electrodes was verified by a linear  $I$ - $V$  relationship (ohmic contact), as shown in Figure S2a, Supporting Information. The devices were annealed at 373 K for 1 h in vacuum chamber to further improve electrical and thermal contacts at the electrodes.

**Electrical and Thermal Properties Measurements:** The electrical resistance and thermal conductance of nanoribbons were measured using suspended-pad microdevices. Such suspended nanoribbon configuration not only maximally relieves substrate-imposed strain and trapped-charge influence, but also ensures that, unlike typical thin film measurements, the electrical and heat fluxes flow along the same path during the measurements. Two SiN<sub>x</sub> pads with Pt electrodes were suspended from the Si substrate by long ( $\approx 400 \mu\text{m}$ ) and flexural SiN<sub>x</sub> arms. Pt serpentine electrodes were patterned on the pads to serve as microheater and thermometer. Four additional Pt line electrodes were deposited for four-probe electrical resistance measurements of the nanoribbon sample. Applying a DC current ( $I = 0$ –15  $\mu\text{A}$ ) to the microheater on one pad, the temperature on it (hot pad) was raised by  $\Delta T_h$ . The heat flowed through the nanoribbon to the other pad (cold pad) and raised its temperature by  $\Delta T_c$ . The base temperature of the two pads (global temperature) was controlled with an external heater (Lakeshore 335 temperature controller) and cryogenic compressor cooler (HC-4A, Sumitomo Cryogenics). All the measurements were performed under high vacuum ( $< 10^{-6}$  Torr) in the vacuum chamber. An AC current with a small amplitude  $\approx 500$  nA and frequency  $\approx 1.1$  kHz (199 Hz) was applied to the Pt serpentine electrodes to probe  $\Delta T_h$  ( $\Delta T_c$ ) on the hot (cold) pad using lock-in amplifiers on the basis of the temperature coefficient of resistance of Pt electrodes. The temperature coefficient of resistance of the Pt electrodes at individual temperatures over the temperature range of measurements was calibrated. The thermal conductance of the nanoribbon ( $G$ ) is given by  $G = (P \times \Delta T_c) / (\Delta T_h^2 - \Delta T_c^2)$ ,<sup>[14,35]</sup> where  $P$  is the heating power of a microheater,  $P = I^2 \times (R_h + R_{\text{arm}})$ , and  $R_h$  and  $R_{\text{arm}}$  are the resistance of Pt electrode on the heating pad and suspended arm, respectively. Electrical resistance of the nanoribbon was measured by the four-probe method using a Keithley nanovoltmeter (2182A) and precision current source (6220). The dimensions of nanoribbons were determined from both SEM and AFM. Data errors were estimated from errors in size of the nanoribbon and  $\Delta T_h$  and  $\Delta T_c$  on the pads:  $\approx 8\%$  for thermal conductivity and  $\approx 5\%$  for electrical conductivity.<sup>[14,15,36]</sup> Thermal contact resistance of the devices is negligible as shown in Figure S2b, Supporting Information.

**Inelastic X-Ray Scattering Measurements:** Phonon dispersions of single crystal 1T-TaS<sub>2</sub> were measured using IXS technique. Specifically, phonon dispersion branches along the  $\Gamma$ -M and  $\Gamma$ -K directions were measured using the HERIX X-ray spectrometer at beamline 30-ID-C at the Advanced Photon Source using 23.7 keV ( $\lambda = 0.5226 \text{ \AA}$ ) X-rays with a focused beam spot size of  $\approx 30 \mu\text{m}$ .<sup>[37]</sup> The 1T-TaS<sub>2</sub> single crystal sample was a large bulk flake with a lateral size of 2–3 mm and thickness of 50–100  $\mu\text{m}$ , as shown in Figure S3, Supporting Information. The thickness was selected to obtain the maximum scattering signal in transmission IXS measurements. The flake was adhered onto a copper rod using thermally conductive epoxy, and the rod was then mounted on an evacuated heating stage for rotation in a vacuum chamber. During the measurement, the counting time was in the range of 30–60 s for each energy scan at a constant  $Q$ . The measured energy spectra were fitted using a Gaussian function for the elastic peak and a damped harmonic oscillator function for the phonon peaks.<sup>[38,39]</sup> Figure 3b presents the experimental IXS results, where the phonon energy,  $E = \hbar\omega$ , is plotted versus the magnitude of the wavevector ( $q$ ) along the  $\Gamma$ -M and  $\Gamma$ -K directions in the reciprocal space. Scattering geometry was used to determine the specific polarization of the atomic vibration for these phonon branches. The scattering vector,  $Q$ , is defined by the summation of a Bragg peak position and a small vector as  $Q = G + q$ , where  $G$  is the reciprocal lattice vector, and  $q$  is a wavevector in the 1st Brillouin zone. Therefore, the phonon branches were measured from combinations of  $Q$  and  $q$  with different Bragg peak positions, and the longitudinal and TA

polarizations of phonons were measured separately.<sup>[40,41]</sup> As an example for the phonon branch along  $\Gamma$ -K direction, the LA phonon dispersion was measured at reciprocal-lattice points  $\mathbf{Q}_{\text{LA}} = (1 + \xi, 1 + \xi, 0)$  with  $\xi = 0.05$ – $0.3$ , and the TA phonon dispersion was measured at  $\mathbf{Q}_{\text{TA}} = (\xi, \xi, 4)$ .  $\mathbf{Q}_{\text{LA}}$  and  $\mathbf{Q}_{\text{TA}}$  are the total scattering vectors, and  $\mathbf{q} = (\xi, \xi, 0)$  is the measured phonon wavevectors. In the schematic reciprocal space with  $\xi = 0.15$  as shown in Figure S4a (in Supporting Information), the phonon wavevector of  $\mathbf{q} = (0.15, 0.15, 0)$  is parallel to  $\mathbf{Q}_{\text{LA}}$  and approximately perpendicular to  $\mathbf{Q}_{\text{TA}}$ , which reveals the longitudinal and transverse atomic vibrations with respect to the phonon propagation direction, respectively. Figure S4b, Supporting Information, shows a plot of the experimental energy scan at  $\mathbf{Q}_{\text{TA}} = (0.15, 0.15, 4)$  of the TA branch. The phonon linewidths were extracted from this line shape function convoluted with experimental resolution function. Figure S5, Supporting Information, illustrates the phonon linewidth for dispersive and less dispersive phonon modes in the NCCDW phase of 1T-TaS<sub>2</sub> at 300 K, where the less dispersive phonon modes show more phonon linewidth broadening than the dispersive modes at comparable energies.

**Simulation Methods:** First-principles calculations were performed in the framework of DFT as implemented in the Quantum Espresso (QE) package<sup>[42,43]</sup> with a plane-wave cutoff of 55 Ry. The DFT calculations were carried out using norm-conserving pseudopotentials<sup>[44]</sup> to describe the electron-ion interaction in the local density approximation of the exchange-correlation interaction. The van der Waals correction was considered with the method of dispersion correction of DFT (DFT-D3).<sup>[45]</sup> The fully relaxed lattice constants of  $a = 3.350$  Å and  $c = 5.954$  Å (experimental values:<sup>[46]</sup>  $a = 3.367$  Å,  $c = 5.902$  Å) were obtained. The 3D Fermi surface structure was simulated with the WANNIER90 code<sup>[47]</sup> and visualized with the XCrySDen package.<sup>[48]</sup> An electronic smearing of 0.05 Ry was applied in the calculation to stabilize the system and prevent it from undergoing the CDW transition.<sup>[49,50]</sup> The phonon-electron scattering rates were calculated using the EPW (e-ph coupling using Wannier functions) code<sup>[51–53]</sup> within the QE package<sup>[42,43]</sup> following the procedure described by Li et al.<sup>[8]</sup> The phonon dispersions and e-ph matrix elements were calculated within density functional perturbation theory as implemented in QE on a coarse  $9 \times 9 \times 5$   $\mathbf{q}$  grids and electron band structure on a  $18 \times 18 \times 10$   $\mathbf{k}$  grid. The coarse grid quantities were interpolated to fine  $\mathbf{k}$  and  $\mathbf{q}$  grids of  $45 \times 45 \times 21$  within the EPW package. The phonon-phonon scattering rates were calculated using the D3Q package within the QE.<sup>[54–56]</sup>

## Supporting Information

Supporting Information is available from the Wiley Online Library or from the author.

## Acknowledgements

This work was supported by the Director, Office of Science, Office of Basic Energy Sciences, Materials Sciences and Engineering Division of the U.S. Department of Energy under contract number DE-AC02-05CH11231. J.H. acknowledges support from the National Science Foundation of China (grant 11572040). Theoretical calculations were performed using resources of the National Supercomputer Centre in Guangzhou, which was supported by the Special Program for Applied Research on Super Computation of the NSFC—Guangdong Joint Fund (the second phase) under grant number U1501501. The IXS measurements were performed using the X-ray Operations and Research (XOR) beamline 30-ID (HERIX) at the Advanced Photon Source, Argonne National Laboratory. The authors thank Prof. David Broido and Prof. Chris Dames for helpful discussions.

## Conflict of Interest

The authors declare no conflict of interest.

## Author Contributions

H.L. and C.Y. contributed equally to this work. J.W. conceived the project. H.L. and J.W. designed the experiments. H.L. fabricated devices and performed the thermal and electrical measurements. H.L., B.W., A.A., A.S., and J.H. performed the inelastic X-ray scattering measurements. C.Y. and J.H. performed the theoretical calculation. S.T. grew the single crystal flake of sample. H.L., C.Y., B.W., L.J., F.Y., J.H., and J.W. discussed the data. H.L. and J.W. wrote the draft. All authors contributed to discussing the data and editing the manuscript.

## Keywords

charge density waves, electron-phonon coupling, tantalum disulfide, lattice thermal conductivity

Received: August 6, 2019  
Revised: March 15, 2020  
Published online: April 23, 2020

- [1] J. M. Ziman, *Electrons and Phonons: The Theory of Transport Phenomena in Solids*, Oxford University Press, Oxford **2001**.
- [2] N. W. Ashcroft, N. D. Mermin, *Solid State Physics*, Holt, Rinehart and Winston, New York **1976**.
- [3] F. Giustino, *Rev. Mod. Phys.* **2017**, *89*, 015003.
- [4] B. Liao, B. Qiu, J. Zhou, S. Huberman, K. Esfarjani, G. Chen, *Phys. Rev. Lett.* **2015**, *114*, 115901.
- [5] W. H. Butler, R. K. Williams, *Phys. Rev. B* **1978**, *18*, 6483.
- [6] Q. Zheng, A. B. Mei, M. Tuteja, D. G. Sangiovanni, L. Hultman, I. Petrov, J. E. Greene, D. G. Cahill, *Phys. Rev. Mater.* **2017**, *1*, 065002.
- [7] L. Yang, Y. Tao, J. Liu, C. Liu, Q. Zhang, M. Akter, Y. Zhao, T. T. Xu, Y. Xu, Z. Mao, Y. Chen, D. Li, *Nano Lett.* **2019**, *19*, 415.
- [8] C. Li, N. K. Ravichandran, L. Lindsay, D. Broido, *Phys. Rev. Lett.* **2018**, *121*, 175901.
- [9] B. Sipoš, A. F. Kusmartseva, A. Akrap, H. Berger, L. Forró, E. Tutiš, *Nat. Mater.* **2008**, *7*, 960.
- [10] M. Eichberger, H. Schafer, M. Krumova, M. Beyer, J. Demsar, H. Berger, G. Moriena, G. Sciaini, R. J. D. Miller, *Nature* **2010**, *468*, 799.
- [11] Y. Yu, F. Yang, X. F. Lu, Y. J. Yan, Y.-H. Cho, L. Ma, X. Niu, S. Kim, Y.-W. Son, D. Feng, S. Li, S.-W. Cheong, X. H. Chen, Y. Zhang, *Nat. Nanotechnol.* **2015**, *10*, 270.
- [12] K. Rossnagel, N. V. Smith, *Phys. Rev. B* **2006**, *73*, 073106.
- [13] F. Clerc, C. Battaglia, M. Bovet, L. Despont, C. Monney, H. Cercellier, M. G. Garnier, P. Aebi, H. Berger, L. Forró, *Phys. Rev. B* **2006**, *74*, 155114.
- [14] L. Shi, D. Li, C. Yu, W. Jang, D. Kim, Z. Yao, P. Kim, A. Majumdar, *J. Heat Transfer* **2003**, *125*, 881.
- [15] S. Lee, F. Yang, J. Suh, S. Yang, Y. Lee, G. Li, H. Sung Choe, A. Suslu, Y. Chen, C. Ko, J. Park, K. Liu, J. Li, K. Hippalgaonkar, J. J. Urban, S. Tongay, J. Wu, *Nat. Commun.* **2015**, *6*, 8573.
- [16] I. Lutsyk, M. Rogala, P. Dabrowski, P. Krukowski, P. J. Kowalczyk, A. Busiakiewicz, D. A. Kowalczyk, E. Laciniska, J. Binder, N. Olszowska, M. Kociuszyński, K. Szalowski, M. Gmitra, R. Stepniński, M. Jalachowski, J. J. Kolodziej, A. Wyszomolek, Z. Klusek, *Phys. Rev. B* **2018**, *98*, 195425.
- [17] R. Inada, Y. Ōnuki, S. Tanuma, *Phys. Lett. A* **1979**, *69*, 453.
- [18] M. D. Núñez-Regueiro, J. M. Lopez-Castillo, C. Ayache, *Phys. Rev. Lett.* **1985**, *55*, 1931.
- [19] J. B. Balaguru Rayappan, S. A. C. Raj, N. Lawrence, *Physica B* **2010**, *405*, 3172.
- [20] J. A. Benda, *Phys. Rev. B* **1974**, *10*, 1409.

- [21] L. Lindsay, D. A. Broido, T. L. Reinecke, *Phys. Rev. Lett.* **2013**, *111*, 025901.
- [22] F. Tian, B. Song, X. Chen, N. K. Ravichandran, Y. Lv, K. Chen, S. Sulivan, J. Kim, Y. Zhou, T.-H. Liu, M. Goni, Z. Ding, J. Sun, G. A. G. U. Gamage, H. Sun, H. Ziyee, S. Huyan, L. Deng, J. Zhou, A. J. Schmidt, S. Chen, C.-W. Chu, P. Y. Huang, D. Broido, L. Shi, G. Chen, Z. Ren, *Science* **2018**, *361*, 582.
- [23] J. S. Kang, M. Li, H. Wu, H. Nguyen, Y. Hu, *Science* **2018**, *361*, 575.
- [24] S. Li, Q. Zheng, Y. Lv, X. Liu, X. Wang, P. Y. Huang, D. G. Cahill, B. Lv, *Science* **2018**, *361*, 579.
- [25] D. A. Broido, T. L. Reinecke, *Phys. Rev. B* **2004**, *70*, 081310.
- [26] K. Rossmagel, *J. Phys.: Condens. Matter* **2011**, *23*, 213001.
- [27] K. R. A. Ziebeck, B. Dorner, W. G. Stirling, R. Schollhorn, *J. Phys. F: Met. Phys.* **1977**, *7*, 1139.
- [28] M. Nakano, K. Shibuya, D. Okuyama, T. Hatano, S. Ono, M. Kawasaki, Y. Iwasa, Y. Tokura, *Nature* **2012**, *487*, 459.
- [29] G. Wehmeyer, T. Yabuki, C. Monachon, J. Wu, C. Dames, *Appl. Phys. Rev.* **2017**, *4*, 041304.
- [30] J. A. Tomko, A. Pena-Francesch, H. Jung, M. Tyagi, B. D. Allen, M. C. Demirel, P. E. Hopkins, *Nat. Nanotechnol.* **2018**, *13*, 959.
- [31] K. T. Law, P. A. Lee, *Proc. Natl. Acad. Sci. USA* **2017**, *114*, 6996.
- [32] B. C. Sales, O. Delaire, M. A. McGuire, A. F. May, *Phys. Rev. B* **2011**, *83*, 125209.
- [33] J. W. Park, G. Y. Cho, J. Lee, H. W. Yeom, *Nat. Commun.* **2019**, *10*, 4038.
- [34] H. Liu, H. S. Choe, Y. Chen, J. Suh, C. Ko, S. Tongay, J. Wu, *Appl. Phys. Lett.* **2017**, *111*, 102101.
- [35] S. Lee, K. Hippalgaonkar, F. Yang, J. Hong, C. Ko, J. Suh, K. Liu, K. Wang, J. J. Urban, X. Zhang, C. Dames, S. A. Hartnoll, O. Delaire, J. Wu, *Science* **2017**, *355*, 371.
- [36] J. Zhu, K. Hippalgaonkar, S. Shen, K. Wang, Y. Abate, S. Lee, J. Wu, X. Yin, A. Majumdar, X. Zhang, *Nano Lett.* **2014**, *14*, 4867.
- [37] T. S. Toellner, A. Alatas, A. H. Said, *J. Synchrotron Radiat.* **2011**, *18*, 605.
- [38] A. Alatas, A. H. Said, H. Sinn, G. Bortel, M. Y. Hu, J. Zhao, C. A. Burns, E. Burkel, E. E. Alp, *Phys. Rev. B* **2008**, *77*, 064301.
- [39] F. Weber, R. Hott, R. Heid, K.-P. Bohnen, S. Rosenkranz, J.-P. Castellan, R. Osborn, A. H. Said, B. M. Leu, D. Reznik, *Phys. Rev. B* **2013**, *87*, 245111.
- [40] G. Shirane, S. M. Shapiro, J. M. Tranquada, *Neutron Scattering with a Triple-Axis Spectrometer: Basic Techniques*, Cambridge University Press, Cambridge **2002**.
- [41] J. D. Budai, J. Hong, M. E. Manley, E. D. Specht, C. W. Li, J. Z. Tischler, D. L. Abernathy, A. H. Said, B. M. Leu, L. A. Boatner, R. J. McQueeney, O. Delaire, *Nature* **2014**, *515*, 535.
- [42] P. Giannozzi, S. Baroni, N. Bonini, M. Calandra, R. Car, C. Cavazzoni, D. Ceresoli, G. L. Chiarotti, M. Cococcioni, I. Dabo, A. D. Corso, S. D. Gironcoli, S. Fabris, G. Fratesi, R. Gebauer, U. Gerstmann, C. Gougoussis, A. Kokalj, M. Lazzeri, L. Martin-Samos, N. Marzari, F. Mauri, R. Mazzarello, S. Paolini, A. Pasquarello, L. Paulatto, C. Sbraccia, S. Scandolo, G. Sclauzero, A. P. Seitsonen, A. Smogunov, P. Umari, R. M. Wentzcovitch, *J. Phys.: Condens. Matter* **2009**, *21*, 395502.
- [43] P. Giannozzi, O. Andreussi, T. Brumme, O. Bunau, M. B. Nardelli, M. Calandra, R. Car, C. Cavazzoni, D. Ceresoli, M. Cococcioni, N. Colonna, I. Carnimeo, A. D. Corso, S. D. Gironcoli, P. Delugas, R. A. DiStasio, A. Ferretti, A. Floris, G. Fratesi, G. Fugallo, R. Gebauer, U. Gerstmann, F. Giustino, T. Gorni, J. Jia, M. Kawamura, H.-Y. Ko, A. Kokalj, E. Küçükbenli, M. Lazzeri, M. Marsili, N. Marzari, F. Mauri, N. L. Nguyen, H.-V. Nguyen, A. Otero-de-la-Roza, L. Paulatto, S. Poncé, D. Rocca, R. Sabatini, B. Santra, M. Schlipf, A. P. Seitsonen, A. Smogunov, I. Timrov, T. Thonhauser, P. Umari, N. Vast, X. Wu, S. Baroni, *J. Phys.: Condens. Matter* **2017**, *29*, 465901.
- [44] D. R. Hamann, *Phys. Rev. B* **2013**, *88*, 085117.
- [45] S. Grimme, J. Antony, S. Ehrlich, H. Krieg, *J. Chem. Phys.* **2010**, *132*, 154104.
- [46] Y. Liu, R. Ang, W. J. Lu, W. H. Song, L. J. Li, Y. P. Sun, *Appl. Phys. Lett.* **2013**, *102*, 192602.
- [47] A. A. Mostofi, J. R. Yates, G. Pizzi, Y.-S. Lee, I. Souza, D. Vanderbilt, N. Marzari, *Comput. Phys. Commun.* **2014**, *185*, 2309.
- [48] A. Kokalj, *Comput. Mater. Sci.* **2003**, *28*, 155.
- [49] N. F. Hinsche, K. S. Thygesen, *2D Mater.* **2017**, *5*, 015009.
- [50] D. L. Duong, M. Burghard, J. C. Schön, *Phys. Rev. B* **2015**, *92*, 245131.
- [51] F. Giustino, M. L. Cohen, S. G. Louie, *Phys. Rev. B* **2007**, *76*, 165108.
- [52] J. Noffsinger, F. Giustino, B. D. Malone, C.-H. Park, S. G. Louie, M. L. Cohen, *Comput. Phys. Commun.* **2010**, *181*, 2140.
- [53] S. Poncé, E. R. Margine, C. Verdi, F. Giustino, *Comput. Phys. Commun.* **2016**, *209*, 116.
- [54] M. Lazzeri, S. de Gironcoli, *Phys. Rev. Lett.* **1998**, *81*, 2096.
- [55] L. Paulatto, F. Mauri, M. Lazzeri, *Phys. Rev. B* **2013**, *87*, 214303.
- [56] G. Fugallo, M. Lazzeri, L. Paulatto, F. Mauri, *Phys. Rev. B* **2013**, *88*, 045430.